# ADAPTIVE RESOLUTION OF FINE SCALES IN MODES OF MICROSTRUCTURED OPTICAL FIBERS *

JAY GOPALAKRISHNAN †, JACOB GROSEK ‡, GABRIEL PINOCHET-SOTO†, AND PIETER VANDENBERGE†

**Abstract.** An adaptive algorithm for computing eigenmodes and propagation constants of optical fibers is proposed. The algorithm is built using a dual-weighted residual error estimator. The residuals are based on the eigensystem for leaky hybrid modes obtained from Maxwell equations truncated to a finite domain after a transformation by a perfectly matched layer. The adaptive algorithm is then applied to compute practically interesting modes for multiple fiber microstructures. Emerging microstructured optical fibers are characterized by complex geometrical features in their transverse cross-section. Their leaky modes, useful for confining and propagating light in their cores, often exhibit fine scale features. The adaptive algorithm automatically captures these features without any expert input. The results also show that confinement losses of these modes are captured accurately on the adaptively found meshes.

**Key words.** optical fibers, finite element adaptivity, mode solving, vector hybrid leaky modes, mode confinement losses, microstructured fibers

**MSC codes.** 65N30, 78A10

## 1. Introduction.

Microstructured optical fibers with complex features are increasingly being fabricated and used [6]. An important consideration in their design is their confinement loss or radiation loss. This loss can be extracted from a complex eigenvalue of an eigenproblem arising from the Maxwell system governing the propagation of light within optical fibers. The corresponding eigenfunctions are practically interesting since they form the leaky modes of fibers capable of propagating substantial portions of the input energy through the fiber. The electric fields of these modes generally have both transverse and longitudinal vector components, so they are also referred to as "hybrid modes" [30]. The purpose of this paper is to give an adaptive algorithm for capturing such modes with sufficient accuracy. The algorithm is based on the mathematical technique of dual-weighted residual (DWR) error estimators [1]. We detail how to apply this approach to a finite element discretization of the eigenproblem for hybrid modes combined with a domain truncation after a transformation by the perfectly matched layer (PML) [2, 5].

Not all microstructured fiber designs use the same physical mechanism for guiding light. Some fibers use confinement by anti-resonant reflection effects [23, 8, 15] while others use confinement by resonances of guided modes, total internal reflection, and photonic confinement within defects of periodic arrangements [11, 14, 22]. The diversity of these physical mechanisms necessitate expert guidance in each fiber's numerical simulation, thus posing challenges in creating general purpose simulation tools for these fibers. This paper contributes to addressing this challenge. Specifically, several practically useful leaky modes of varied microstructured fibers have been found to exhibit fine-scale ripples in varied locations. As shown in [31], accuracy of computed

*Submitted to the editors 04/04/2024.

**Funding:** This work was supported in part by AFOSR Grant FA9550-23-1-0103 and NSF Grant 2245077. The work also benefited from activities organized under the auspices of NSF RTG Grant 2136228.

† The Fariborz Maseeh Department of Mathematics + Statistics, Portland State University, PO Box 751, Portland, OR, USA (gjay@pdx.edu, gpin2@pdx.edu, piet2@pdx.edu).

‡ Directed Energy Directorate, Air Force Research Laboratory, 3550 Aberdeen Ave SE, Kirtland Air Force Base, Albuquerque, NM (AFRL.RDL.OrgBox@us.af.mil).

confinement losses depend on resolving such fine-scale features. To do so without expert insight and to facilitate design optimization, an algorithm that can automatically detect such fine-scale features accompanied by appropriate mesh refinement is useful. This paper provides such an algorithm, basing it on sound mathematical principles independent of fiber design. A prior work proposing a goal-oriented adaptivity strategy for computing losses accurately is [35], but as best as we can see, the goal functional proposed there is not a continuous functional and we do not know how to make their technique mathematically rigorous. Instead, we develop an alternate approach based on the ideas in [12] which directly target the eigenvalue error.

The eigenvalues of the Maxwell system for hybrid modes are squares of the physical propagation constant $\beta$ of the modes. Confinement loss of a fiber is a scalar multiple of the imaginary part of $\beta$. Typical values of $\beta$ have real parts of the order of $10^6$ and imaginary parts, $\mathrm{Im}(\beta)$, that can range in orders of magnitude $10^{-6}$ to $10^3$, depending on the fiber and operating wavelength. To get around this large variation in order of magnitudes, instead of a mere length scaling, we perform a nondimensionalization of the Maxwell system (see Section 2) akin to the process of going from Helmholtz to a Schrödinger problem. Then, instead of $\beta^2$, we compute a nondimensional $Z^2$, of unit order of magnitude, in the complex plane. Applying this approach to varied fibers, we find that an adaptive algorithm tailored to reduce the error in $Z^2$ also appears to get the confinement loss accurately and capture the above-mentioned fine-scale ripples. Whether a mathematically rigorous algorithm tailored specifically to reduce the error in loss can be found, and if so, whether it will do better, is an issue for further research.

The basis for DWR-based adaptive algorithms is developed in terms of optimal control in the review [1]. Roughly speaking, their idea is that the error in a quantity of interest can be estimated by an element-wise residual (which treats local error contributions), weighted by the solution of a dual problem (which takes global error transport into account). DWR algorithms specific for eigenvalues have been outlined for elliptic problems in [12, 26]. We choose the DWR error estimation technique because our eigenproblem is nonselfadjoint and because our eigensolver readily gives the dual solution (left eigenvector) in addition to the solution (the eigenvalue and the right eigenvector). Not incurring extra costs for solving the dual problem in this case makes the DWR technique an efficient choice. To apply the DWR methodology to our Maxwell eigenvalue application, we bring in an additional technique, namely the use of a regular decomposition. The resulting theory is summarized in a single self-contained theorem and proof in Section 3 giving the error estimator expression, after which we describe our adaptive algorithm. Later sections clearly reveal the efficacy of the algorithm for computing leaky modes of complex fibers. In particular, Section 4 is devoted to verifying the correctness of the methodology using a Bragg fiber for which mode solutions in exact closed form are available.

Modes are not available in analytic closed form for the three other fibers we consider. Their geometries are displayed in Figures 1b, 1c and 1d. Antiresonant fibers (ARF) such as those displayed in Figures 1b and 1c hold great promise due to their potential for low loss propagation in their large hollow cores (filled with air which has negligible optical nonlinearities). Negative-curvature hollow-core ARF, like that in Figure 1b, but with eight thin capillaries were studied experimentally in [15]. The Nested Anti-Resonant Nodeless Fiber (NANF), whose microstructure design is illustrated in Figure 1c, has capillaries each containing a smaller capillary ring within it, was studied in [23], where it was projected to have improved (lower) losses compared to the previous ARF designs, like that in Figure 1b. Photonic bandgap (PBG)

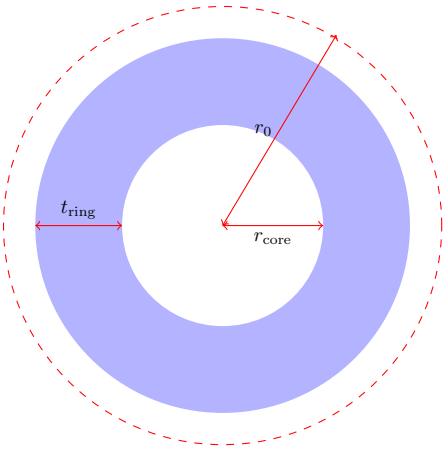


(a) Geometry of the Bragg fiber.

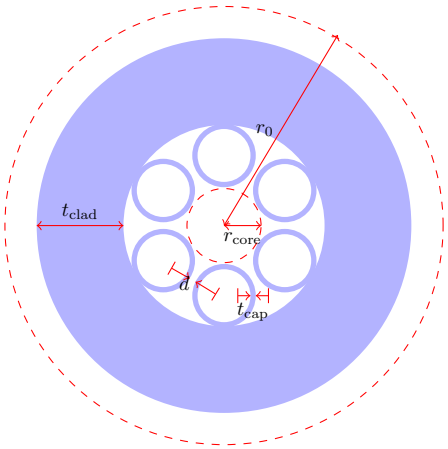


(b) Geometry of the ARF fiber.

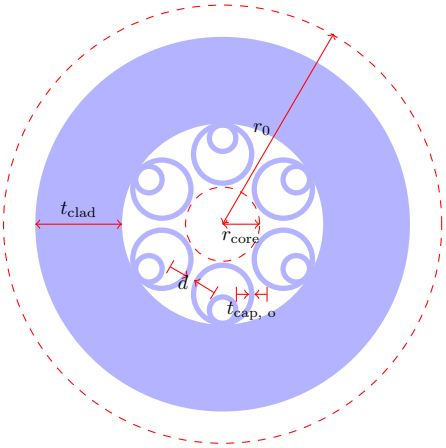


(c) Geometry of the NANF fiber.

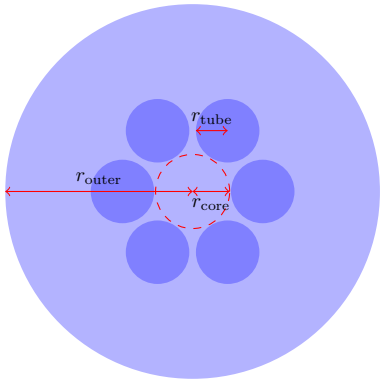


(d) Geometry of the PBG fiber.

Figure 1: Transverse geometries of the microstructured fibers (not to scale) studied in this work. White regions indicate air and shades of blue indicate dielectric materials with higher refractive indices.

fibers like that in Figure 1d form another category of popular microstructure fiber designs [14, 22, 24, 7, 19] gaining utility, particularly where all-solid fibers are preferred. The geometry of the PBG fiber used here contains a single layer of hexagonally arranged high-index inclusions, a design shown to have the same transmission minima as more complex multi-layer devices [19]. Note that it is not the goal of this paper to discuss the relative merits of various microstructures. Rather, our purpose in considering the diverse designs in Figure 1 is to demonstrate the general purpose utility of the proposed algorithm. As we shall see, the modes of all these fibers have fine-scale features that the algorithm is able to successfully resolve.

The remainder of this paper is organized as follows. Section 2 describes the mathematical formulation of the eigenproblem starting from Maxwell equations. All details of the PML and the finite element discretization are included there. The DWR error estimator, its theoretical basis, and the adaptivity algorithm appears in Section 3. The methodology is verified in Section 4 using a model Bragg fiber and its semi-analytically computable propagation constants. Finally, we conclude in Section 5 by applying the algorithm to the above-mentioned three practically important fiber microstructures.

**2. The eigenproblem for leaky Maxwell modes.** In this section, we quickly outline the steps to derive a weak formulation for outgoing leaky hybrid modes of an optical fiber using a perfectly matched layer. The resulting system, labeled (2.12) below, is the eigenproblem we shall solve in the remaining sections. We explain how the variable coefficients in (2.12) are derived since they are important for the implementation of the error estimators discussed later.

The governing equation for light propagation in an optical fiber is the time-harmonic Maxwell system for the electric field, $\hat{E}$, and the magnetic field, $\hat{H}$, where all time variations are of the form $e^{-\imath\omega t}$ for some frequency $\omega > 0$,

$$-\imath\omega\mu\hat{H} + \nabla \times \hat{E} = 0, \tag{2.1a}$$

$$\imath\omega\varepsilon\hat{E} + \nabla \times \hat{H} = 0, \tag{2.1b}$$

for all $(x_0, x_1, x_2) \in \mathbb{R}^3$, where $+x_2$ is the field's propagation direction, $\varepsilon$ represents the electric permittivity and $\mu$ denotes the magnetic permeability, and $\nabla \times \cdot$ is the three-dimensional curl operator. We assume that $\mu > 0$ is isotropic and constant, an assumption that holds well for most optical materials. However, $\varepsilon$ may have anisotropies of the following form $\varepsilon = \operatorname{diag}(\varepsilon_\tau, \varepsilon_\tau, \varepsilon_2) = \left[\begin{smallmatrix} \varepsilon_\tau \delta & 0 \\ 0 & \varepsilon_2 \end{smallmatrix}\right]$ where $\varepsilon_\tau$ and $\varepsilon_2$ are positive scalar functions and $\delta$ denotes the $2 \times 2$ identity matrix. The assumption of isotropy in $x_0x_1$ plane is made only for simplicity and can be easily relaxed for the considerations in this paper.

We are interested in Maxwell solutions that propagate along the longitudinal direction $x_2$, which represents the direction of translational symmetry of our optical fiber. Thus, we seek solutions of the form

$$\hat{E}(x_0, x_1, x_2) = E(x_0, x_1)\, e^{\imath\beta x_2}, \qquad \hat{H}(x_0, x_1, x_2) = H(x_0, x_1)\, e^{\imath\beta x_2}, \tag{2.2}$$

for some *propagation constant* $\beta$ and vector fields $E, H$ to be determined. By using unit vectors $e_0, e_1, e_2 \in \mathbb{R}^3$ in the coordinate directions, the *transverse* part of a vector field $F = F(x_0, x_1, x_2)$ is its projection into the span of $e_0$ and $e_1$, denoted by $F_\tau$, so that $F = F_\tau + F_2 e_2$ where $F_2$ is the *longitudinal* component of $F$. Let $R$ denote the 90 degree rotation operator that maps any transverse field $F_\tau = F_0 e_0 + F_1 e_1$ to $RF_\tau = F_1 e_0 - F_0 e_1$. Define the divergence and the scalar-valued curl for transverse fields by $\operatorname{div} F_\tau = \partial_0 F_0 + \partial_1 F_1$ and $\operatorname{curl}(F_\tau) = \operatorname{div}(RF_\tau)$. The rotated gradient of a scalar field $\phi$ is defined by $\operatorname{rot}\phi = R\ \operatorname{grad}(\phi)$. Next, we substitute (2.2) into (2.1), decompose $E$ and $H$ into transverse and longitudinal components, and use the identity $\nabla \times \left(u\, e^{\imath\beta x_2}\right) = \left(e^{\imath\beta x_2} \operatorname{curl} u_\tau\right) e_2 + e^{\imath\beta x_2} \left(\operatorname{rot} u_2 - \imath\beta R u_\tau\right)$. Then, eliminating $H_2$ and $H_\tau$ and simplifying (see e.g., [31, Appendix A.1] for more details), the Maxwell system reduces to a system coupling the transverse electric field $E_\tau$ and a scaled longitudinal component of the field $\varphi = \imath\beta E_2$, which reads as follows:

$$\operatorname{rot}\operatorname{curl} E_\tau - \omega^2 \varepsilon_\tau \mu E_\tau + \operatorname{grad}\varphi = -\beta^2 E_\tau, \tag{2.3a}$$

$$\varepsilon_2 \mu \varphi + \operatorname{div}(\varepsilon_\tau \mu E_\tau) = 0, \tag{2.3b}$$

This is a mixed eigensystem for the eigenvalue $-\beta^2$ where the second equation may be viewed as a constraint.

The physical dimensions of the fiber's transverse cross-section are in micrometers, while practical propagation constants are usually of the order of $10^6$, so a nondimensionalization is useful. Let $\varepsilon_0$ and $\mu_0$ be the electric permittivity and magnetic permeability of the vacuum, respectively. Let $k^2 = \omega^2\varepsilon_0\mu_0$. Define the transverse and longitudinal refractive indices by $n_\tau^2 = \varepsilon_\tau\mu_0/\varepsilon_0\mu$ and $n_2^2 = \varepsilon_2\mu_0/\varepsilon_0\mu$. Now, using a characteristic length scale $L$ for the fiber cross-section, we rescale $(x_0, x_1) \mapsto (x_0/L, x_1/L)$ and consider all the unknown functions in the rescaled coordinates. Outside some finite radius (of the same order as $L$) in the transverse plane we assume that the refractive index $n(x_0, x_1)$ is isotropic and equal to a constant $n_0$. Using an *index well* defined by $V(x_0, x_1) = L^2k^2(n_0^2 - n_\tau(x_0, x_1)^2)$ in the rescaled nondimensional coordinates, the system (2.3) leads us [31, Appendix A.2] to the following non-dimensional equations:

$$\operatorname{rot}\operatorname{curl} E_\tau + VE_\tau + \operatorname{grad}\varphi = Z^2E_\tau, \qquad \text{in } \mathbb{R}^2, \tag{2.4a}$$

$$n_2^2\varphi + \operatorname{div}(n_\tau^2 E_\tau) = 0, \qquad \text{in } \mathbb{R}^2, \tag{2.4b}$$

where $Z^2 = L^2(k^2n_0^2 - \beta^2)$ is a nondimensional eigenvalue.

The system (2.4) must be supplemented with boundary conditions. We shall use the outgoing condition at infinity, described below. Before discussing it however, consider the case where all fields have decayed to some negligible magnitude (as in a guided mode) at the boundary of a large enough disk $\Omega$ in the $x_0x_1$-plane, sufficiently far from the compact support of the index well $V$. Multiplying the first equation of (2.4) by a vector test function $F$ and the second by a scalar test function $\psi$, integrating by parts, and using $E_\tau = 0$ and $\varphi = 0$ on $\partial\Omega$, we obtain the following weak formulation. Find $E_\tau \in \mathring{H}(\operatorname{curl}, \Omega)$ and $\varphi \in \mathring{H}^1(\Omega)$, satisfying

$$\int_\Omega (\operatorname{curl} E_\tau)(\operatorname{curl} F) + \int_\Omega VE_\tau \cdot F + \int_\Omega (\operatorname{grad}\varphi)\cdot F = Z^2\int_\Omega E_\tau \cdot F, \tag{2.5a}$$

$$\int_\Omega n_2^2\varphi\psi - \int_\Omega n_\tau^2 E_\tau \cdot \operatorname{grad}\psi = 0, \tag{2.5b}$$

for all $F \in \mathring{H}(\operatorname{curl}, \Omega)$ and all $\psi \in \mathring{H}^1(\Omega)$. Here $\mathring{H}(\operatorname{curl}, \Omega)$ denotes the space of square-integrable vector fields whose curl is also square integrable and whose tangential component along $\partial\Omega$ vanishes and $\mathring{H}^1(\Omega)$ denotes square-integrable scalar functions which vanish on $\partial\Omega$ all of whose first-order derivatives are also square integrable on $\Omega$. Prior works featuring similar weak formulations include [16, 17, 31, 32].

Leaky modes satisfy (2.4) and also satisfy the condition at infinity that the mode must be *outgoing*. To explain this, first note that the fiber's translational symmetry in $x_2$-direction and the absence of inhomogeneities in $r^2 \equiv x_0^2 + x_1^2 > R^2$ for some finite cylindrical radius $R$, implies that we can use separation of variables to obtain a series expansion of solution components in terms of solutions of the Bessel equation in $r$ and sines and cosines in the angular variable $\theta$. From among all solutions to the Bessel equation, when $Z$ is a positive real number, the outgoing requirement selects Hankel functions of the first kind, $H_\ell^{(1)}$. Hence the radial variation of all terms in the solution representation are of the form $H_\ell^{(1)}(Zr)$ as $r \to \infty$ (see e.g., [5] or [10, eq. (23)]). For complex values of $Z$, the outgoing condition requires that the solution is expressible in terms of the analytic continuations into $\mathbb{C}$, from the positive real axis, of the same

Hankel functions $H_\ell^{(1)}(Zr)$. A practically convenient method to impose this condition is through a perfectly matched layer (PML) [2] which transforms coordinates so that the solution of (2.4), while unaltered in a bounded region where $V$ is inhomogeneous, becomes exponentially decaying outside. The exponential decay allows us to truncate the infinite domain $\mathbb{R}^2$ in (2.4) to a bounded computational domain $\Omega$ as in (2.5). To view PML as a complex coordinate transformation [20, 5], we let $\tilde{x} := \Phi(x)$ where $\Phi(x) = x\,\eta(r)/r$ for some complex-valued function $\eta(r)$ to be specified later. Here $x = [x_0, x_1]^\mathsf{T}$, $\tilde{x} = [\tilde{x}_0, \tilde{x}_1]^\mathsf{T}$, and $r = \sqrt{x_0^2 + x_1^2}$. Put $x_\perp = [x_1, -x_0]^\mathsf{T}$. Consider the $2 \times 2$ Jacobian matrix whose entries are $J_{ij} := \partial \tilde{x}_i / \partial x_j$. Simple computations give that with $\zeta(r) = \eta(r)/r$, we have

$$J = \frac{\zeta'}{r} x x^\mathsf{T} + \zeta \delta, \qquad J^{-1} = \frac{1}{\eta'}\delta + \frac{\zeta'}{\eta\eta'} x_\perp x_\perp^\mathsf{T}, \qquad \det(J) = \zeta\eta'. \tag{2.6}$$

We transform scalar-valued functions $\psi$ and vector-valued functions $\Psi$ in the following distinct ways:

$$\tilde{\psi} = \psi \circ \Phi^{-1}, \qquad \tilde{\Psi} = J^{-\mathsf{T}} \Psi \circ \Phi^{-1}. \tag{2.7}$$

By placing a tilde over a differential operator, we indicate that the derivative is being taken with respect to $\tilde{x}$ rather than $x$. Calculations using the chain rule shows that the matrix $D\Psi$ whose $(i,j)$th entry equals $\partial_j \Psi_i$ satisfies $\tilde{\partial}_j \tilde{\Psi}_i = [J^{-\mathsf{T}}\ D\Psi\ J^{-1}]_{ij} + \sum_l \Psi_l\, \partial^2 x_l / \partial\tilde{x}_j \partial\tilde{x}_i$. Relating its skew symmetric part to the curl and applying (2.6), we obtain

$$\tilde{\operatorname{curl}}\, \tilde{\Psi} = \frac{1}{(\eta')^2} \left(1 + \frac{\zeta' r^2}{\eta}\right) (\operatorname{curl} \Psi) \circ \Phi^{-1} \tag{2.8a}$$

Similarly, the chain rule applied to $\tilde{\psi} = \psi \circ \Phi^{-1}$ gives

$$\tilde{\operatorname{grad}}\ \tilde{\psi} = J^{-\mathsf{T}} (\operatorname{grad} \psi) \circ \Phi^{-1}. \tag{2.8b}$$

In the complexified domain $\tilde{\Omega} = \Phi(\Omega)$, we solve the analogue of system (2.5) obtained by replacing curl by $\tilde{\operatorname{curl}}$, grad by $\tilde{\operatorname{grad}}$, and $\Omega$ by $\tilde{\Omega}$, namely

$$\int_{\tilde{\Omega}} (\tilde{\operatorname{curl}}\, \tilde{E}_\tau)(\tilde{\operatorname{curl}}\, \tilde{F}) + \int_{\tilde{\Omega}} V \tilde{E}_\tau \cdot \tilde{F} + \int_{\tilde{\Omega}} (\operatorname{grad} \tilde{\varphi}) \cdot \tilde{F}) = Z^2 \int_{\tilde{\Omega}} \tilde{E}_\tau \cdot \tilde{F}, \tag{2.9a}$$

$$\int_{\tilde{\Omega}} n_2^2 \tilde{\varphi}\tilde{\psi} - \int_{\tilde{\Omega}} n_\tau^2 \tilde{E}_\tau \cdot \operatorname{grad} \tilde{\psi} = 0. \tag{2.9b}$$

where $\tilde{E}_\tau, \tilde{F}, \tilde{\varphi}$ and $\tilde{\psi}$ are obtained from $E_\tau, F, \varphi$ and $\psi$ using (2.7).

Since it is more convenient to compute on a domain with real coordinates, we now transform the equations of (2.9) back to $\Omega$ using the identities in (2.6) and (2.8), e.g.,

$$\int_{\tilde{\Omega}} (\tilde{\operatorname{curl}}\, \tilde{E}_\tau)(\tilde{\operatorname{curl}}\, \tilde{F}) = \int_{\tilde{\Omega}} \kappa\ \operatorname{curl} E_\tau\ \operatorname{curl} F,$$

with

$$\kappa = \frac{\zeta}{(\eta')^3} \left(1 + \frac{\zeta' r^2}{\eta}\right)^2. \tag{2.10}$$

Also defining

$$\gamma = \zeta\eta' J^{-\mathsf{T}} J^{-1}, \tag{2.11}$$

and performing similar transformations for other terms in (2.9), we are led to a weak formulation with PML. Namely, we find $E_\tau \in \mathring{H}(\mathrm{curl}, \Omega)$ and $\varphi \in \mathring{H}^1(\Omega)$, satisfying

$$a(E_\tau, F) + c(\varphi, F) = Z^2\ m(E_\tau, F), \qquad \text{for all } F \in \mathring{H}(\mathrm{curl}, \Omega), \tag{2.12a}$$

$$b(E_\tau, \psi) + d(\varphi, \psi) = 0, \qquad \text{for all } \psi \in \mathring{H}^1(\Omega), \tag{2.12b}$$

where

$$a(E_\tau, F) = (\kappa \,\mathrm{curl}\, E_\tau, \mathrm{curl}\, F)_\Omega + (V\gamma E_\tau, F)_\Omega, \tag{2.13a}$$

$$b(E_\tau, \psi) = \left(n_\tau^2 \gamma E_\tau, \mathrm{grad}\, \psi\right)_\Omega, \qquad c(\phi, F) = (\gamma\, \mathrm{grad}\, \phi, F)_\Omega, \tag{2.13b}$$

$$d(\phi, \psi) = -\left(n_2^2 \zeta \eta' \phi, \psi\right)_\Omega, \qquad m(E_\tau, F) = (\gamma E_\tau, F)_\Omega. \tag{2.13c}$$

Here $(\cdot,\cdot)_\Omega$ denotes the (complex) inner product of $L^2(\Omega)$ or its Cartesian products and we have used the conjugates of test functions in (2.9). The system (2.12) completes the description of the weak formulation for computing leaky modes, except for a prescription of $\eta(r)$.

There are multiple ways to choose $\eta(r)$, as can be seen from the literature [5, 10, 13, 21]. We use a two-dimensional analogue of an expression in [13]. To describe it, we fix $\Omega$ to be a disk of radius $r_1$, assume that support of $V$ is contained in a disk of radius $r_0 < r_1$, and that a cylindrical PML is set in the annular region $r_0 < r < r_1$. Let $0 < \alpha$ be the PML strength parameter. We set

$$\eta(r) = 1 + \imath\phi(r), \tag{2.14a}$$

where

$$\phi(r) = \begin{cases} 0, & \text{if } r < r_0, \\ \alpha \dfrac{\displaystyle\int_{r_0}^{r} (s-r_0)^2 (s-r_1)^2 \,\mathrm{d}s}{\displaystyle\int_{r_0}^{r_1} (s-r_0)^2 (s-r_1)^2 \,\mathrm{d}s}, & \text{if } r_0 < r < r_1. \end{cases} \tag{2.14b}$$

This together with $\zeta(r) = \eta(r)/r$ defines all quantities that appear in (2.12).

We conclude this section by describing the finite element discretization of (2.12) that we shall employ. First, mesh $\Omega$ by a geometrically conforming finite element mesh of triangles, and denote the mesh by $\Omega_h$. On a triangle $K$, let $P_p(K)$ denote the space of polynomials in two variables of degree at most $p$. The degree $p$ and the maximal element diameter $h = \max_{K\in\Omega_h} \mathrm{diam}(K)$ determine the richness of the discretization. The Lagrange finite element space on $\Omega_h$, for any $p \geq 0$ is defined by $V_h = \{\psi : \psi|_K \in P_{p+1}(K) \text{ for all } K \in \Omega_h,\ \psi \text{ is continuous}\}$. The Nédélec finite element space [20] is the set of all vector fields $F$ on $\Omega$ whose tangential components are continuous across element interfaces and whose restrictions to each element $K \in \Omega_h$ is a polynomial of the form $F|_K \in P_p(K)^2 + \left[\begin{smallmatrix} x_1 \\ -x_0 \end{smallmatrix}\right] P_p(K)$. We use curved triangles next to curved material interfaces, in which case, as usual, the polynomial space within such an element is replaced by the pullback of the above-indicated polynomial spaces from a reference triangle. The Galerkin discretization using these spaces give the discrete eigenproblem that solves for $E_{\tau,h} \in N_h$ and $\varphi_h \in V_h$ such that

$$a(E_{\tau,h}, F) + c(\varphi_h, F) = Z_h^2\ m(E_{\tau,h}, F), \qquad \text{for all } F \in N_h, \tag{2.15a}$$

$$b(E_{\tau,h}, \psi) + d(\varphi_h, \psi) = 0, \qquad \text{for all } \psi \in V_h. \tag{2.15b}$$

All results of computations described in later sections are obtained by solving (2.15).

**3. The error estimator for eigenvalues.** In this section, we describe the *a posteriori* error estimator for the previously described eigenproblem. It is obtained by applying the DWR technique [1, 12, 26]. Although only eigenproblems with second-order elliptic operators were considered in these references, the generality of their technique is well recognized. Even though our eigenproblem involves a non-elliptic operator, the same approach applies, as we shall now see.

Let $H = \mathring{H}(\mathrm{curl}, \Omega) \times \mathring{H}^1(\Omega)$ and $H_h = N_h \times V_h$. Putting $\lambda = Z^2$, $u = (E_\tau, \varphi) \in H$, and $v = (F, \psi) \in H$, we restate the eigenproblem (2.12) as

$$A(u, w) = \lambda B(u, w), \qquad \|u\|_H = 1, \tag{3.1}$$

for all $w \in H$ with

$$A(u, v) = a(E_\tau, F) + c(\varphi, F) + b(E_\tau, \psi) + d(\varphi, \psi), \quad B(u, v) = m(E_\tau, F),$$

with $a, b, c, d, m$ as in (2.13). Viewing $u$ as a right eigenfunction, we also assume that there is a corresponding left eigenfunction $0 \neq \tilde{u} = (\tilde{E}_\tau, \tilde{\varphi}) \in H$ satisfying

$$A(\tilde{v}, \tilde{u}) = \lambda B(\tilde{v}, \tilde{u}), \quad \text{for all } \tilde{v} \in H, \tag{3.2a}$$

$$B(u, \tilde{u}) = 1. \tag{3.2b}$$

Next, consider the Galerkin discretizations of these eigenproblems, considered previously in (2.15). Using the same type of normalizations as in (3.1)–(3.2), we assume there is a discrete right eigenfunction $u_h = (E_{\tau,h}, \varphi_h) \in H_h$ and a discrete left eigenfunction $\tilde{u}_h = (\tilde{E}_{\tau,h}, \tilde{\varphi}_h) \in H_h$ satisfying

$$A(u_h, w) = \lambda_h B(u_h, w), \qquad \|u_h\|_H = 1, \tag{3.3}$$

for all $w \in H_h$ and

$$A(\tilde{v}, \tilde{u}_h) = \lambda_h B(\tilde{v}, \tilde{u}_h), \quad \text{for all } \tilde{v} \in H_h, \tag{3.4a}$$

$$B(u_h, \tilde{u}_h) = 1. \tag{3.4b}$$

where $\lambda_h = Z_h^2$.

Next, to describe the error estimators, using the coefficients $\kappa$ and $\gamma$ in (2.10) and (2.11), we first set element-wise residuals. Let $\|\cdot\|_D$ denote the $L^2(D)$-norm for a subset $D$ such as $T \in \Omega_h$ or its boundary $\partial T$. Let $h_T$ denote the diameter of $T$. On an interior mesh edge, let $\nu$ denote a unit normal of arbitrarily fixed orientation. Jumps of multivalued functions at the element interfaces are denoted by $[\![\cdot]\!]$; so, for example, $[\![(n_\tau^2 \gamma E_{\tau,h}) \cdot \nu]\!]$ denotes the jump of the normal ($\nu$) component of $n_\tau^2 \gamma E_{\tau,h}$ across an interior edge. Using this notation, define (unweighted) element-wise residuals by

$$\rho_{T,1}^2 = h_T^2 \left\| \mathrm{rot}(\kappa \,\mathrm{curl}\, E_{\tau,h}) + V\gamma E_{\tau,h} + \gamma \,\mathrm{grad}\, \varphi_h - Z_h^2 \gamma E_{\tau,h} \right\|_T^2 + \frac{h_T}{2} \left\| [\![\kappa \,\mathrm{curl}\, E_{\tau,h}]\!] \right\|_{\partial T \setminus \partial\Omega}^2, \tag{3.5a}$$

$$\rho_{T,2}^2 = h_T^2 \left\| \mathrm{div}(\gamma \,\mathrm{grad}\, \varphi_h + V\gamma E_{\tau,h} - Z_h^2 \gamma E_{\tau,h}) \right\|_T^2 + \frac{h_T}{2} \left\| [\![(\gamma \,\mathrm{grad}\, \varphi_h + V\gamma E_{\tau,h} - Z_h^2 \gamma E_{\tau,h}) \cdot \nu]\!] \right\|_{\partial T \setminus \partial\Omega}^2, \tag{3.5b}$$

$$\rho_{T,3}^2 = h_T^2 \left\| \mathrm{div}(n_\tau^2 \gamma E_{\tau,h}) + n_2^2 \zeta \eta' \varphi_h \right\|_T^2 + \frac{h_T}{2} \left\| [\![(n_\tau^2 \gamma E_{\tau,h}) \cdot \nu]\!] \right\|_{\partial T \setminus \partial\Omega}^2, \tag{3.5c}$$

and define weights arising from the dual eigenfunction components by

$$\tilde{\omega}_{T,1} = \|\operatorname{curl}\tilde{E}_\tau\|_T, \qquad \tilde{\omega}_{T,2} = \|\tilde{E}_\tau\|_T, \qquad \tilde{\omega}_{T,3} = \|\operatorname{grad}\tilde{\varphi}\|_T. \tag{3.5d}$$

Similarly, using complex conjugates of the coefficients, we define analogous element-wise residuals for the dual problem,

$$\begin{aligned}\tilde{\rho}^2_{T,1} &= h_T^2 \left\|\operatorname{rot}(\bar{\kappa}\operatorname{curl}\tilde{E}_{\tau,h}) + n_\tau^2\bar{\gamma}\operatorname{grad}\tilde{\varphi}_h + V\bar{\gamma}\tilde{E}_{\tau,h} - \bar{Z}_h^2\bar{\gamma}\tilde{E}_{\tau,h}\right\|_T^2 \\ &\quad + \frac{h_T}{2}\left\| \left[\!\left[\bar{\kappa}\operatorname{curl}\tilde{E}_{\tau,h}\right]\!\right] \right\|^2_{\partial T\setminus\partial\Omega},\end{aligned} \tag{3.5e}$$

$$\begin{aligned}\tilde{\rho}^2_{T,2} &= h_T^2 \left\|\operatorname{div}(n_\tau^2\bar{\gamma}\operatorname{grad}\tilde{\varphi}_h + V\bar{\gamma}\tilde{E}_{\tau,h} - \bar{Z}_h^2\bar{\gamma}\tilde{E}_{\tau,h})\right\|_T^2 \\ &\quad + \frac{h_T}{2}\left\| \left[\!\left[(n_\tau^2\bar{\gamma}\operatorname{grad}\tilde{\varphi}_h + V\bar{\gamma}\tilde{E}_{\tau,h} - \bar{Z}_h^2\bar{\gamma}\tilde{E}_{\tau,h})\cdot\nu\right]\!\right] \right\|^2_{\partial T\setminus\partial\Omega},\end{aligned} \tag{3.5f}$$

$$\tilde{\rho}^2_{T,3} = h_T^2 \left\|\operatorname{div}(\bar{\gamma}\tilde{E}_{\tau,h}) + n_2^2\bar{\zeta}\bar{\eta}'\tilde{\varphi}_h\right\|_T^2 + \frac{h_T}{2}\left\| \left[\!\left[(\bar{\gamma}\tilde{E}_{\tau,h})\cdot\nu\right]\!\right] \right\|^2_{\partial T\setminus\partial\Omega}, \tag{3.5g}$$

and weights generated by the right eigenfunction:

$$\omega_{T,1} = \|\operatorname{curl}E_\tau\|_T, \qquad \omega_{T,2} = \|E_\tau\|_T, \qquad \omega_{T,3} = \|\operatorname{grad}\varphi\|_T. \tag{3.5h}$$

Using these, we define a local element-wise error indicator by

$$\eta_T = \sum_{i=1}^{3} \rho_{T,i}\,\tilde{\omega}_{T,i} + \tilde{\rho}_{T,i}\,\omega_{T,i}, \tag{3.5i}$$

for each $T \in \Omega_h$. A practical version of this idealized error indicator will be given later: see (3.13).

The adaptive algorithm we use is motivated by the next result (Theorem 3.1 below), which gives a global reliability estimate for the error indicator $\eta_T$. We prove it using the DWR approach laid out in [1, 12, 26], but bring in an additional ingredient to decompose $H(\operatorname{curl})$ approximation errors into locally controllable gradients and a regular remainder using the results of [27]. As usual, we make a "saturation assumption," which here takes the form that the discretizations considered are fine enough so that

$$\left(\max_{x\in\Omega}\|\gamma(x)\|_2\right)\,\|E_\tau - E_{\tau,h}\|_\Omega\,\|\tilde{E}_\tau - \tilde{E}_{\tau,h}\|_\Omega\, < 1 \tag{3.6}$$

holds. The assumption is likely to hold on reasonable meshes since the product of errors on the left is expected to go to zero faster than the field error as $h$ approaches zero. Hereon, we use $A \lesssim B$ to indicate that there exists a meshsize ($h$) independent constant $C > 0$ (possibly dependent on shape regularity of the mesh) such that the inequality $A \le CB$ holds.

THEOREM 3.1. *Suppose the vectors $u = (E_\tau, \varphi)$, $u_h = (E_{\tau,h}, \varphi_h)$, $\tilde{u} = (\tilde{E}_\tau, \tilde{\varphi})$, $\tilde{u}_h = (\tilde{E}_{\tau,h}, \tilde{\varphi}_h)$, solve* (3.1), (3.2), (3.3) *and* (3.4), *respectively, with accompanying exact and discrete eigenvalues $\lambda$ and $\lambda_h$. Suppose also that* (3.6) *holds. Then the error in eigenvalue can be bounded by the error indicators defined in* (3.5) *by*

$$|\lambda - \lambda_h| \lesssim \sum_{T\in\Omega_h} \eta_T. \tag{3.7}$$

*Proof.* Let

$$\rho(\tilde{v}) = A(u_h, \tilde{v}) - \lambda_h B(u_h, \tilde{v}), \qquad \tilde{\rho}(v) = A(v, \tilde{u}_h) - \lambda_h B(v, \tilde{u}_h)$$

for any $v, \tilde{v} \in H$. Also let $\sigma = B(u - u_h, \tilde{u} - \tilde{u}_h)/2$. The argument is based [12] on the identity

$$(\lambda - \lambda_h)(1 - \sigma) = \frac{1}{2}\rho(\tilde{u} - \tilde{v}_h) + \frac{1}{2}\tilde{\rho}(u - v_h) \tag{3.8}$$

which holds for any $\tilde{v}_h, v_h \in H_h$. Its proof is elementary:

$$\begin{aligned}
\rho(\tilde{u} - \tilde{v}_h) + \tilde{\rho}(u - v_h) &= A(u_h, \tilde{u}) - \lambda_h B(u_h, \tilde{u}) \\
&\quad + A(u, \tilde{u}_h) - \lambda_h B(u, \tilde{u}_h), && \text{by (3.3) \& (3.4)}, \\
&= (\lambda - \lambda_h)\big[B(u_h, \tilde{u}) + B(u, \tilde{u}_h)\big], && \text{by (3.1) \& (3.2)}, \\
&= (\lambda - \lambda_h)\big[B(u_h - u, \tilde{u} - \tilde{u}_h) + 2\big], && \text{by (3.2b) \& (3.4b)},
\end{aligned}$$

from which (3.8) follows for any $v_h, \tilde{v}_h \in H_h$.

We proceed setting $v_h = (\Pi_h E_\tau, I_h \varphi_h)$, where $I_h$ is the Scott-Zhang interpolant [29] and $\Pi_h$ is the quasi-interpolant defined in [27]. The results of [27] prove that there is an $e \in \mathring{H}^1(\Omega)$ and $z \in [\mathring{H}^1(\Omega)]^2$ such that

$$E_\tau - \Pi_h E_\tau = z + \operatorname{grad} e, \tag{3.9a}$$

$$h_T^{-1}\|e\|_T + \|\operatorname{grad} e\|_T \lesssim \|E_\tau\|_{\Omega_T}, \tag{3.9b}$$

$$h_T^{-1}\|z\|_T + \|\operatorname{grad} z\|_T \lesssim \|\operatorname{curl} E_\tau\|_{\Omega_T}. \tag{3.9c}$$

where $\Omega_T$ is the union of all elements connected to $T$. Using this decomposition and integrating by parts,

$$\begin{aligned}
\tilde{\rho}(u - v_h) &= A(u - v_h, \tilde{u}_h) - \lambda_h B(u - v_h, \tilde{u}_h) \\
&= A((z + \operatorname{grad} e, \varphi - I_h\varphi), (\tilde{E}_{\tau,h}, \tilde{\varphi}_h)) - Z_h^2 \left(\gamma(z + \operatorname{grad} e), \tilde{E}_{\tau,h}\right)_\Omega \\
&= \left(\kappa \operatorname{curl} z, \operatorname{curl} \tilde{E}_{\tau,h}\right)_\Omega \\
&\quad + \left(V\gamma(z + \operatorname{grad} e) + \gamma \operatorname{grad}(\varphi - I_h\varphi) - Z_h^2\gamma(z + \operatorname{grad} e), \tilde{E}_{\tau,h}\right)_\Omega \\
&\quad + \left(n_\tau^2\gamma(z + \operatorname{grad} e), \operatorname{grad} \tilde{\varphi}_h\right)_\Omega - \left(n_2^2\zeta\eta'(\varphi - I_h\varphi), \tilde{\varphi}_h\right)_\Omega \\
&= \sum_{T \in \Omega_h} \Big[ \left(z \cdot t, \bar{\kappa} \operatorname{curl} \tilde{E}_{\tau,h}\right)_{\partial T} \\
&\qquad + \left(z, \operatorname{rot} \bar{\kappa} \operatorname{curl} \tilde{E}_{\tau,h} + n_\tau^2\bar{\gamma} \operatorname{grad} \tilde{\varphi}_h + V\bar{\gamma}\tilde{E}_{\tau,h} - \bar{Z}_h^2\bar{\gamma}\tilde{E}_{\tau,h}\right)_T \\
&\qquad + \left(e, (n_\tau^2\bar{\gamma} \operatorname{grad} \tilde{\varphi}_h + V\bar{\gamma}\tilde{E}_{\tau,h} - \bar{Z}_h^2\bar{\gamma}\tilde{E}_{\tau,h}) \cdot \nu\right)_{\partial T} \\
&\qquad - \left(e, \operatorname{div}(n_\tau^2\bar{\gamma} \operatorname{grad} \tilde{\varphi}_h + V\bar{\gamma}\tilde{E}_{\tau,h} - \bar{Z}_h^2\bar{\gamma}\tilde{E}_{\tau,h})\right)_T \\
&\qquad + (\varphi - I_h\varphi, (\bar{\gamma}\tilde{E}_{\tau,h}) \cdot \nu)_{\partial T \setminus \partial\Omega} \\
&\qquad - (\varphi - I_h\varphi, \operatorname{div}(\bar{\gamma}\tilde{E}_{\tau,h}) + n_2^2\bar{\zeta}\bar{\eta}'\tilde{\varphi}_h)_T \Big],
\end{aligned} \tag{3.10}$$

where $t$ and $\nu$ are, respectively, the unit counterclockwise tangent and the unit outward normal vectors on element boundaries. To bound the element boundary

terms in the sum above, we use the well-known local trace estimate $h_T^{-1}\|w\|_{\partial T}^2 \lesssim h_T^{-2}\|w\|_T^2 + \|\operatorname{grad} w\|_T^2$ which holds for any $w \in H^1(T)$ on any element $T$ of a shape-regular mesh. Using it, the first term in the sum (3.10) can be bounded by

$$\begin{aligned}\Big|\sum_{T\in\Omega_h}(z\cdot t, \bar\kappa \operatorname{curl}\tilde E_{\tau,h})_{\partial T}\Big| &\lesssim \sum_{T\in\Omega_h}\left(h_T^{-1/2}\|z\|_{\partial T}\right)\left(h_T^{1/2}\left\|[\![\bar\kappa \operatorname{curl}\tilde E_{\tau,h}]\!]\right\|_{\partial T\setminus\partial\Omega}\right)\\ &\lesssim \sum_{T\in\Omega_h}\left(h_T^{-1}\|z\| + \|\operatorname{grad} z\|_T\right)\tilde\rho_{T,1}\\ &\lesssim \sum_{T\in\Omega_h}\|\operatorname{curl} E_\tau\|_{\Omega_T}\,\tilde\rho_{T,1},\end{aligned}$$

where we have used (3.9c). The second term is also bounded using (3.9c):

$$\left(z, \operatorname{rot}\bar\kappa\operatorname{curl}\tilde E_{\tau,h} + n_\tau^2\bar\gamma\operatorname{grad}\tilde\varphi_h + V\bar\gamma\tilde E_{\tau,h} - \bar Z_h^2\bar\gamma\tilde E_{\tau,h}\right)_T \lesssim \|\operatorname{curl} E_\tau\|_{\Omega_T}\,\tilde\rho_{T,1}.$$

Similarly, applying (3.9b), we find

$$\begin{aligned}&\Big|\sum_{T\in\Omega_h}\left(e, (n_\tau^2\bar\gamma\operatorname{grad}\tilde\varphi_h + V\bar\gamma\tilde E_{\tau,h} - \bar Z_h^2\bar\gamma\tilde E_{\tau,h})\cdot\nu\right)_{\partial T}\Big|\\ &\quad\lesssim \sum_{T\in\Omega_h}\left(h_T^{-1/2}\|e\|_{\partial T}\right)\left(h_T^{1/2}\left\|\left[\!\left[(n_\tau^2\bar\gamma\operatorname{grad}\tilde\varphi_h + V\bar\gamma\tilde E_{\tau,h} - \bar Z_h^2\bar\gamma\tilde E_{\tau,h})\cdot\nu\right]\!\right]\right\|_{\partial T}\right)\\ &\quad\lesssim \sum_{T\in\Omega_h}\left(h_T^{-1}\|e\|_T + \|\operatorname{grad} e\|\right)\tilde\rho_{T,2} \lesssim \sum_{T\in\Omega_h}\|E_\tau\|_{\Omega_T}\,\tilde\rho_{T,2}\end{aligned}$$

and

$$\left(e, \operatorname{div}(n_\tau^2\bar\gamma\operatorname{grad}\tilde\varphi_h + V\bar\gamma\tilde E_{\tau,h} - \bar Z_h^2\bar\gamma\tilde E_{\tau,h})\right)_T \le h_T^{-1}\|e\|_T\,\tilde\rho_{T,2} \lesssim \|E_\tau\|_{\Omega_T}\,\tilde\rho_{T,2}.$$

For the last two terms in (3.10), we use the well-known property of $I_h$,

$$h_T^{-1}\|\varphi - I_h\varphi\|_T + \|\operatorname{grad}(\varphi - I_h\varphi)\|_T \lesssim \|\operatorname{grad}\varphi\|_{\Omega_T}$$

in place of (3.9) and apply Cauchy-Schwarz inequality in a similar fashion as above. Gathering bounds on all terms, we arrive at

$$\tilde\rho(u - v_h) \lesssim \sum_{T\in\Omega_h}\omega_{T,1}\,\tilde\rho_{T,1} + \omega_{T,2}\,\tilde\rho_{T,2} + \omega_{T,3}\,\tilde\rho_{T,3}. \tag{3.11}$$

Next, consider the other residual, $\rho(\tilde u - \tilde v_h)$. Setting $\tilde v_h = (\mathit{\Pi}_h\tilde E_\tau, I_h\tilde\varphi_h)$ and applying the same type of arguments, we prove that

$$\rho(u - \tilde v_h) \lesssim \sum_{T\in\Omega_h}\tilde\omega_{T,1}\,\rho_{T,1} + \tilde\omega_{T,2}\,\rho_{T,2} + \tilde\omega_{T,3}\,\rho_{T,3}. \tag{3.12}$$

Finally, note that the definitions of $\sigma$ and $B$ imply

$$\begin{aligned}2\sigma = B(u - u_h, \tilde u - \tilde u_h) &= m(E_\tau - E_{\tau,h}, \tilde E_\tau - \tilde E_{\tau,h})\\ &= (\gamma(E_\tau - E_{\tau,h}), \tilde E_\tau - \tilde E_{\tau,h})_\Omega < 1,\end{aligned}$$

where the last inequality is due to (3.6). Thus $1 - \sigma > 1/2$. Using this, together with (3.12) and (3.11) within the identity (3.8), the stated estimate follows. ∎

We conclude this section by describing the *adaptive algorithm* we implemented. First, to make the error indicator $\eta_T$ practical, following the heuristics of [12, Remark 10], we take the next step of replacing the unknown weights $\tilde{\omega}_{T,i}$ and $\omega_{T,i}$ by a computable analogue that is likely to be close in value, namely

$$\begin{aligned} \tilde{\omega}_{T,1}^{(h)} &= \|\operatorname{curl} \tilde{E}_{\tau,h}\|_T, \qquad \tilde{\omega}_{T,2}^{(h)} = \|\tilde{E}_{\tau,h}\|_T, \qquad \tilde{\omega}_{T,3}^{(h)} = \|\operatorname{grad} \tilde{\varphi}_h\|_T, \\ \omega_{T,1}^{(h)} &= \|\operatorname{curl} E_{\tau,h}\|_T, \qquad \omega_{T,2}^{(h)} = \|E_{\tau,h}\|_T, \qquad \omega_{T,3}^{(h)} = \|\operatorname{grad} \varphi_h\|_T. \end{aligned}$$

Replacing the weights in (3.5i) by these, we obtain the practical element-wise error indicator we use:

$$\eta_T^{(h)}(\lambda_h, u_h, \tilde{u}_h) = \sum_{i=1}^{3} \rho_{T,i}\, \tilde{\omega}_{T,i}^{(h)} + \tilde{\rho}_{T,i}\, \omega_{T,i}^{(h)}. \tag{3.13}$$

The next practicality involves aggregating estimators when multiple eigenvalues $\lambda_h^{(\ell,k)}$ are found clustered, together with their left and right eigenvectors $\tilde{u}_h^{(\ell,k)}, u_h^{(\ell,k)}$, $k = 1, \ldots, K_\ell$, in the $\ell$-th adaptive iteration. Then, we simply compute the element-wise maximum of the error indicators for each eigenvalue. Namely, we compute $\eta_T^{(\ell,k)} = \eta_T^{(h)}(\lambda_h^{(\ell,k)}, u_h^{(\ell,k)}, \tilde{u}_h^{(\ell,k)})$ using (3.13) and set

$$\eta_T^{(\ell)} = \max_{k=1,\ldots,K_\ell} \eta_T^{(\ell,k)}. \tag{3.14}$$

An element $T' \in \Omega_h^{(\ell)}$ is marked for refinement if

$$\eta_{T'}^{(\ell)} > \theta \max_{T \in \Omega_h} \eta_T^{(\ell)}, \tag{3.15}$$

where $\theta$ is an input refinement threshold parameter. This is used in Algorithm 3.1, which summarizes the adaptive strategy we implemented.

We conclude this section by specifying the parameters we used in Algorithm 3.1 and ensuing computations. We use NGSolve [28] for Nédélec and Lagrange finite elements and for assembly of the eigensystem. It supports curved triangles, with a specifiable order of polynomial curving, as well as high-order Nédélec and Lagrange elements. Algorithm 3.1 can use any sparse eigensolver. In our computations, we use the FEAST contour integral eigensolver [25, 9] (whose specific application to leaky modes is also detailed in [10, Section A.4]), which takes as input a search region enclosed by a simple closed contour (denoted by $D$ in the algorithm). We use circular contours of small enough radius centered at $\hat{\lambda}_h^{(n)} = \frac{1}{K_n} \sum_{k=1}^{K_n} \lambda_h^{(n,k)}$, i.e., these centers track changes within each adaptive iteration and $D$ may therefore vary with iteration number $\ell$. How aggressively the refinements are made is determined by the parameter $\theta$. For our computations, we used $\theta = 0.75$, a value determined by trial and error to give us a good balance between localization of the refinements and a steady increase in the number of degrees of freedom (d.o.f.s). So as to represent all eigenmodes of the eigenvalue cluster on the same mesh, the algorithm uses a marking strategy based on the maximum of the error indicators generated by each eigenmode. Other marking strategies are possible, as in [33, 1, 12]. As a stopping criterion, we set the maximum number of degrees of freedom to $N_{\max} = 2 \times 10^6$ in our numerical experiments.

**Algorithm 3.1** Adaptive algorithm for leaky modes

**Input:** Initial mesh $\Omega_h^{(0)}$, refinement threshold $\theta$, an eigenvalue search region $D \subseteq \mathbb{C}$, and the maximum permitted number of degrees of freedom $N_{\max}$.

**Result:** Final adaptively refined mesh $\Omega_h^{(\ell)}$, and a cluster of eigenvalues $\Lambda_h^{(\ell)}$ contained in $D$ obtained using $\Omega_h^{(\ell)}$.

**for** $\ell \leftarrow 0, 1, 2, \ldots$ **do**
  SOLVE: Assemble the system in (3.3) using $\Omega_h^{(\ell)}$ and solve it using a sparse eigensolver to obtain a cluster of eigenvalues $\lambda_h^{(\ell,k)} = (Z_h^{(\ell,k)})^2$ contained in $D$, and the corresponding right and left eigenvectors $u_h^{(\ell,k)}$ and $\tilde{u}_h^{(\ell,k)}$ for $k = 1, \ldots, K_\ell$.
  ESTIMATE: Compute error indicators $\eta_T^{(\ell)}$ using (3.14) for each element $T \in \Omega_h^{(\ell)}$.
  MARK elements for refinement based on (3.15) and input $\theta$.
  REFINE marked elements in $\Omega_h^{(\ell)}$ (as well as surrounding elements as needed to obtain mesh conformity) to generate the next mesh $\Omega_h^{(\ell+1)}$.
  **if** *number of degrees of freedom on* $\Omega_h^{(\ell+1)} > N_{\max}$ **then**
    break
**return** $\Omega_h^{(\ell)}$ *and* $\Lambda_h^{(\ell)}$

**4. Verification by Bragg fiber.** It is well known [34, 18] that an air waveguide surrounded by a higher index cladding can have modes that propagate energy and are primarily confined in the air core region. This design is a type of hollow-core Bragg fiber such that its transverse cross-section consists of a glass ring in infinite air (see Figure 1a). Such fibers were more recently re-examined in [3, 31] where the dielectric ring was viewed as an "anti-resonant" layer. In particular, the results of [31] demonstrated that certain fine-scale features in the higher index region must be resolved to obtain confinement losses with acceptable accuracy. There, these fine features were also definitively shown to be not an artifact of numerical approximations, nor of the PML, since they were captured both by semi-analytic methods and by numerical computations.

These prior studies make the Bragg configuration an ideal example for verifying our adaptive strategy. Because we can semi-analytically compute the exact eigenvalue $\lambda = Z^2$ for this geometry, we are able to study the history of actual eigenvalue errors as the adaptive mesh refinement proceeds. Moreover, starting with an unbiased mesh that disregards the above-mentioned prior knowledge of the fine-scale features in the modes, we investigate if the (deliberately blinded) adaptivity process is able to sense these features automatically and guide refinement to capture them.

In our numerical experiments for this fiber, we use the following settings for parameters (recalling that the parameters were defined in Section 3). The length scale in nondimensionalization is set to $L = 1.5 \times 10^{-5}$ m. The operating wavelength is determined by setting $k = \frac{2\pi}{1.7} \times 10^6$ m$^{-1}$. The refractive index is a piecewise-constant function whose values are $n_{\text{air}} = 1.00027717$ in the air regions and $n_{\text{glass}} = 1.43881648$ in the glass ring. The following non-dimensionalized radii are used: the air core has radius $r_{\text{core}} = 2.7183$; the glass ring starts at $r_{\text{core}}$ and has an outer radius $r_{\text{outer}} = 3.385$, with a thickness of $t_{\text{ring}} = 0.66666667$; the outer air region starts at $r_{\text{outer}}$ and extends to $r_0 = 4.385$, with a thickness of $t_{\text{air}} = 1.0$; and the PML starts at $r_0$ and extends to $r_1 = 8.05166666$, with a thickness of $t_{\text{PML}} = 3.66666667$. The

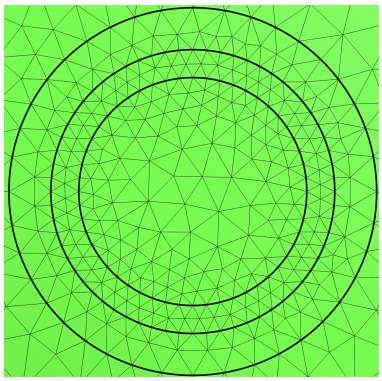

(a) Initial mesh for the Bragg fiber, zoomed in near the glass ring.

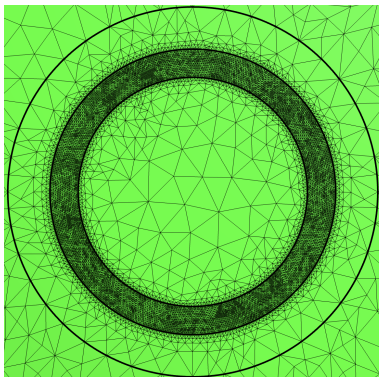

(b) Final mesh for the Bragg fiber after the adaptive algorithm.

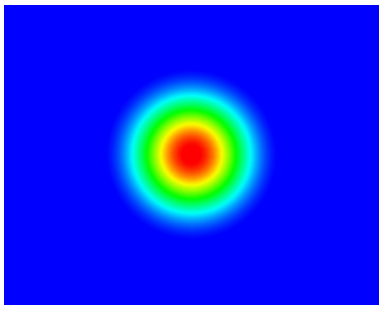

(c) Intensity of the full electric field (right eigenmode) at the final mesh.

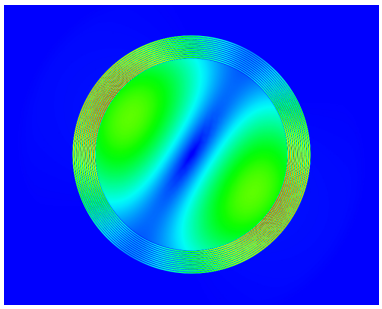

(d) Magnitude of the longitudinal component ($\varphi_h$) of the eigenmode.

Figure 2: Results from the adaptive algorithm applied to a Bragg fiber.

PML strength (recall (2.14)) is set to $\alpha = 2.0$. We set polynomial degree of $p = 6$ to define the discretization (2.15).

The resulting mode at the conclusion of an adaptive iteration is displayed in Figure 2. Clearly, in the initial mesh, visible in Figure 2a, element sizes are more or less the same within the glass ring and in the air regions (with $h \approx 0.1$ in nondimensional units). The computational subdomains are visible there, demarcated by thicker lines, showing the air core, the glass ring, the outer air enclosure, and an outermost circle indicating the beginning of the PML. The final mesh produced by the adaptive algorithm, given in Figure 2b, shows strong local refinement within the glass ring. The total electric field intensity at the final iterate (Figure 2c) reveals a mode highly localized in the air core as expected. In this figure, the fine-scale features are too small in amplitude to be visible. However, examining the magnitude of the smaller longitudinal electric field component in Figure 2d, fine-scale ripples in the glass ring are visible. These were pointed out in [31] from results of semi-analytical computations. We see that the algorithm guided the adaptive refinement process to capture these fine-scale features automatically. Here and throughout, we use a blue-to-red colormap for mode intensity plots, where blue indicates zero and red indicates

the maximal value. Color scale is omitted from such plots since the modes are only defined up to a scalar multiple.

Next, we turn to examine the accuracy of the computed eigenvalue. The results are in Figure 3. The exact nondimensional eigenvalue we aim to approximate, obtained from semi-analytical computations, is $Z^2 = 0.80953881 + 0.00170153i$, and the exact eigenvalue cluster is the singleton containing it, $\Lambda = \{Z^2\}$. The discrete eigenvalue cluster $\Lambda_h$ is computed by providing a circular contour to FEAST centered around the exact eigenvalue. When the eigensolver converged, $\Lambda_h$ generally had two elements, matching the multiplicity of the exact eigenvalue. Let the Hausdorff distance between two sets $\Upsilon_1$ and $\Upsilon_2$ be denoted by

$$d(\Upsilon_1, \Upsilon_2) = \max\Big( \sup_{\gamma_1 \in \Upsilon_1} \operatorname{dist}(\gamma_1, \Upsilon_2), \sup_{\gamma_2 \in \Upsilon_2} \operatorname{dist}(\gamma_2, \Upsilon_1) \Big).$$

We report the convergence of the discrete eigenvalues in $\Lambda_h$ to $\Lambda$ using the Hausdorff distance in Figure 3.

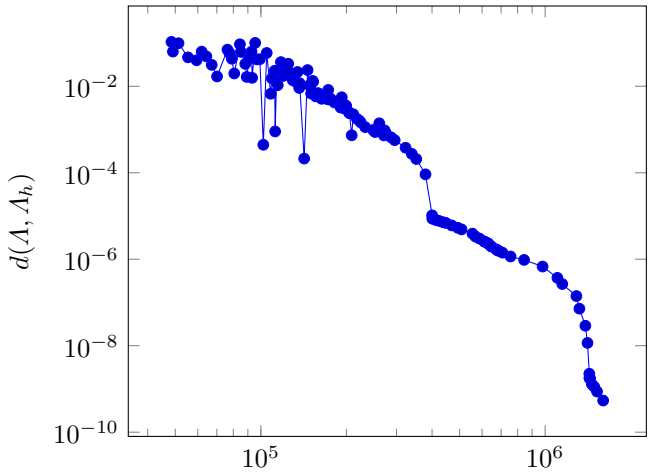


Figure 3: Convergence history of the cluster of discrete eigenvalues to the exact eigenvalue for the Bragg fiber, during the adaptive mesh refinement.

The confinement loss (CL) of a fiber, in decibels per meter (dB/m), is calculated from the propagation constant $\beta$ by

$$\mathrm{CL} = \mathrm{Im}(\beta) \times \frac{20}{\ln(10)}. \tag{4.1}$$

In the $\ell$th adaptive iteration, prior to computing the confinement loss for a cluster of eigenvalues $Z_h \in \Lambda_h^{(\ell)}$ that converge to the same value, we average the nondimensional $Z_h$-values in the cluster to obtain their mean value $\hat{Z}_h$, then set $\hat{\beta}_h^{(\ell)} = (k^2 n_0^2 - \hat{Z}_h^2/L^2)^{1/2}$, and compute $\mathrm{CL}_\ell$ by replacing $\beta$ with $\hat{\beta}_h^{(\ell)}$ in (4.1). The difference between this value and the exact confinement loss value calculated from the exact $\beta$ is reported in Figure 4. Excellent agreement is found as adaptive iterations progress.

Finally, we report on how the error estimator compares to the actual eigenvalue error (which can be computed for this example since an exact solution is available).

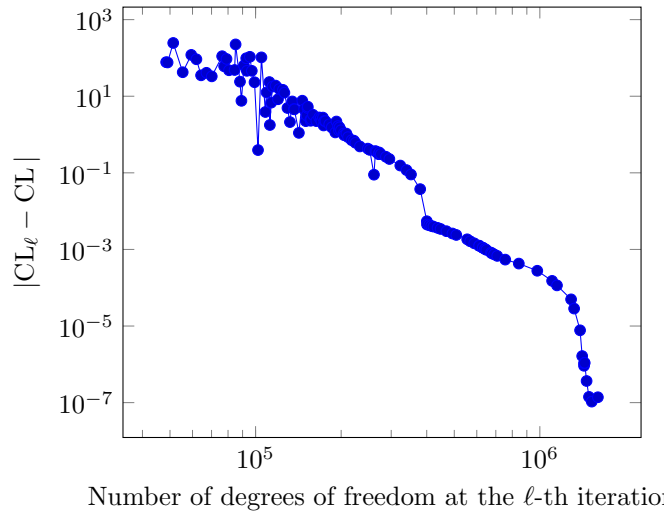


Figure 4: Convergence history of the confinement loss (see (4.1)) for the Bragg fiber, during the adaptive mesh refinement.

Consider the ratio of the the global error of the computed eigenvalues to the global error estimator, i.e., at the $\ell$th iteration, let

$$\text{Efficiency}(\ell) = \max_{\lambda_h \in \Lambda_h^{(\ell)}} |\lambda_h - \lambda| \Big/ \left( \sum_{T \in \Omega_h^{(\ell)}} (\eta_T^{(\ell)})^2 \right)^{1/2}, \tag{4.2}$$

where $\lambda = Z^2$ is the above-mentioned known exact eigenvalue. These values, for each mesh in the history of adaptive refinements, are plotted in Figure 5. As can be seen from Figure 5, these values oscillates greatly in a preasymptotic regime, after which they stabilize somewhat, hovering well below one. On all meshes except one, these values are below one, indicating that the eigenvalue error is bounded by the computed error estimator, i.e., the estimator is quite reliable. However, we also observe that the efficiency values are not very close to the perfect value of one. Such efficiencies are comparable to previous reports [12] that lead us to not anticipate perfect efficiencies for the DWR estimator, even for textbook nonselfadjoint eigenproblems simpler than ours.

**5. Three microstructured fibers.** In this section, we report the results obtained using our adaptive algorithm on three different microstructured fiber designs.

**5.1. A hollow-core anti-resonant fiber.** First, we consider the ARF microstructure in Figure 1b, motivated by studies in [15, 23] of anti-resonant nodeless tube-lattice fiber. This fiber has a hollow-core surrounded by glass capillaries (modeled as) embedded into a glass cladding.

The parameters used for the simulation are as follows. Length scale is $L = 1.5 \times 10^{-5}$ m; operating wavelength is determined by $k = \frac{2\pi}{1.8} \times 10^6$ m$^{-1}$; the refractive index is $n_{\text{air}} = 1.00027717$ in the air core, and $n_{\text{glass}} = 1.44087350$ in the glass ring. The following non-dimensionalized radii and thicknesses are used: the core of the fiber is a circle of radius $r_{\text{core}} = 1.0$; the capillary is defined between an inner

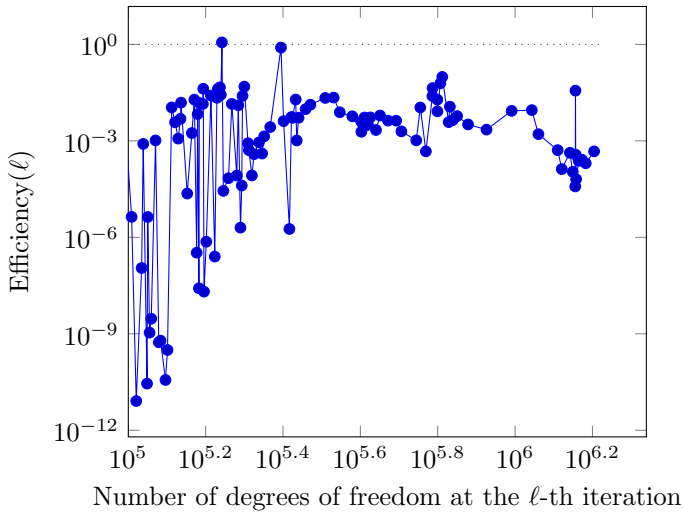


Figure 5: Plot of ratios of eigenvalue error to the estimator (see (4.2)) on each mesh during the adaptive process applied to the Bragg fiber.

radius $r_{\text{cap, i}} = 2.71833333$ and an outer radius $r_{\text{cap, o}} = 3.385$, with a thickness of $t_{\text{cap}} = 0.66666667$; the cladding has an inner radius $r_{\text{clad, i}} = 3.385$ and an outer radius $r_{\text{clad, o}} = 4.05166667$, the thickness of the glass jacket (cladding) is $t_{\text{clad}} = 0.66666667$; the embedding of the capillary into the cladding is given by $e = 0.05952380$, which represents the fraction of the capillary thickness that is submerged in the cladding; the distance between the capillaries is $d = 0.13999999$; the outer layer of air starts at $r_{\text{clad, o}}$ and ends at $r_0 = 4.05166667$, and has a thickness of $t_{\text{air}} = 0.66666667$; the PML region extends from $r_0$ to $r_1 = 7.385$, with a thickness of $t_{\text{PML}} = 3.33333333$. The PML strength (implemented through relation (2.14)) is $\alpha = 2.0$. The algorithm was run with a search region to capture the expected core-localized fundamental mode of this fiber.

The results are portrayed in the images of Figure 6. The initial mesh (Figure 6a) is relatively coarse, with small elements used only to conform to the geometry of the thin glass capillaries and their melding into the cladding. We make the elements in the core region smaller (with $0.2 \lesssim h \lesssim 0.5$), to capture the expected core-localized fundamental mode of this fiber and verify the saturation assumption. The final mesh produced by the adaptivity iteration (Figure 6b) is characterized by unexpectedly strong local refinement in the outer glass cladding where there are no tiny geometrical features to be resolved. This is explained by Figure 6d where we see fine-scale ripples in the high-index cladding for the longitudinal electric field component. The total intensity (Figure 6c) is characterized by a localized profile in the air core. However, because the mode intensity in the core region is orders of magnitude larger than its fine-scale features in the cladding region, one may not realize such cladding ripples exist and are important for accurately resolving the mode loss. The cladding oscillations of the mode intensity are visible when plotting the smaller longitudinal vector component of the mode. The importance of capturing these fine scale features was first pointed out in [31], where an expert "informed mesh" was manually created with enough elements to capture the fine-scale oscillations. Here, we see that the automatic

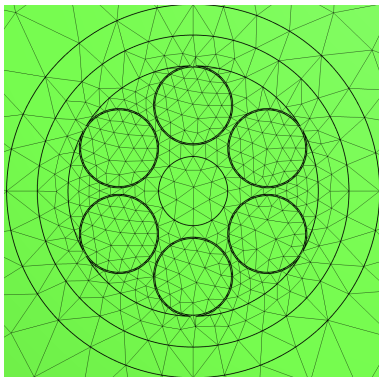

(a) Initial mesh for the ARF geometry.

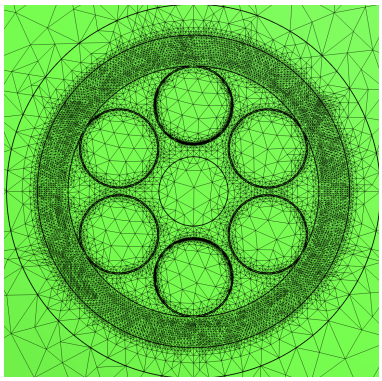

(b) Final mesh for the ARF after the adaptive algorithm

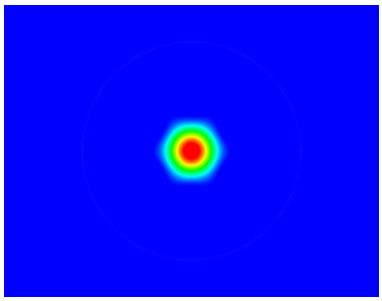

(c) Intensity of the full electric field (right eigenmode) at the final mesh.

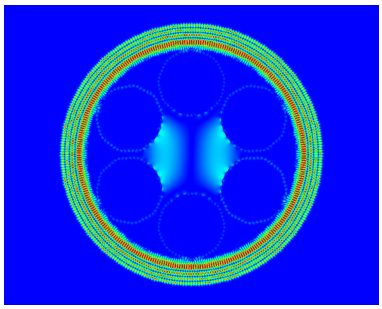

(d) Magnitude of the longitudinal component ($\varphi_h$) of the eigenmode.

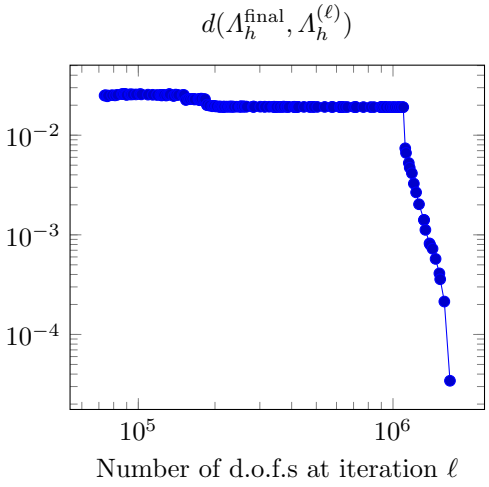


(e) History of adaptive convergence.

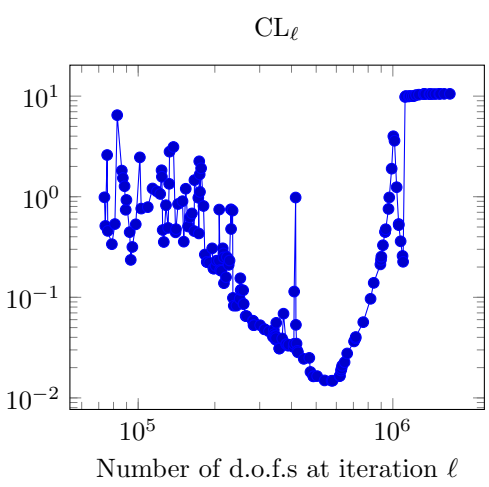


(f) History of computed loss values.

Figure 6: Results from the adaptive algorithm applied to ARF.

adaptive process also points to the necessity of refinements in the same region.

The apparent convergence history during the adaptive process is displayed in Figure 6e. Since we do not have exact eigenvalues for this case, we cannot calculate the eigenvalue errors in each iteration. Instead, we compare the Hausdorff distance between the final output $\Lambda_h^{\text{final}}$ (at the last iteration) with the discrete eigenvalue cluster $\Lambda_h^{(\ell)}$ (with two elements converging to the same number) found at the $\ell$th adaptive iteration. The curve exhibits an overall decreasing trend, even if not a monotonic decrease. The CL values at each iteration are plotted in Figure 6f. We observe convergence of the CL values when the curve flattens out in the last few iterations.

**5.2. A nested anti-resonant nodeless fiber.** Next, we consider the NANF microstructure in Figure 1c, motivated by the studies in [23, 4]. Its main difference with the ARF is that the cladding has a nested structure of capillaries. Since this structure is close to the previously considered ARF, we anticipate that fine-scale mode features of a similar nature to arise here.

We employ the following parameters for the simulation. The length scale is $L = 1.5 \times 10^{-5}$ m; the operating wavelength is determined by $k = \frac{2\pi}{1.8} \times 10^6$ m$^{-1}$; the refractive index is $n_{\text{air}} = 1.00027717$ in the air regions, and $n_{\text{glass}} = 1.44087350$ in the glass ring. We utilize the following non-dimensionalized radii and thicknesses: the core of the fiber is a circle of radius $r_{\text{core}} = 1.0$; the outer capillary is determined by an outer radius $r_{\text{cap, o}} = 0.832$, and a thickness of $t_{\text{cap, o}} = 0.028$; the inner capillary is defined by an inner radius $r_{\text{cap, i}} = 0.4$, and a thickness of $t_{\text{cap, i}} = 0.028$; the cladding has an inner radius $r_{\text{clad}} = 1.33333333$, an outer radius $r_{\text{buffer}} = 2.0$, and a thickness $t_{\text{clad}} = 0.66666667$; the glass ring has an inner radius $r_{\text{inner}} = 2.692$, an outer radius $r_{\text{outer}} = 4.35866667$, and a thickness $t_{\text{clad}} = 1.66666667$; and the PML region starts at $r_{\text{outer}}$ and ends on $r_{\text{PML}} = 7.02533333$. We consider a PML strength (see (2.14)) of value $\alpha = 2.0$.

The results in Figure 7 confirm that fine-scale modal features exist for this fiber as well. The initial mesh (Figure 7a) is relatively coarse, with small elements used only to conform to the geometry of the thin glass capillaries and their melding into the cladding (as in the ARF case). We make the elements in the core region smaller (with $0.2 \lesssim h \lesssim 0.5$), to capture the expected core-localized fundamental mode of this fiber and verify the saturation assumption. Again, the adaptive meshing algorithm found (in Figure 7b) that significant refinements were needed in the outer glass cladding; however, it also determined that some refinements were warranted in the hollow-core near larger capillaries that bound the core. The captured fine-scale modal features are visible in Figure 7d. The convergence of the eigenvalues and CL values during the adaptive process are illustrated in Figures 7e and 7f.

**5.3. A photonic bandgap fiber.** Finally, we consider the PBG microstructure design in Figure 1d, previously studied in [24, 7, 19]. The lattice arrangement of the dielectric rods in the fiber can be modified to change the guiding properties of the fiber. We base our model parameters on the descriptions in [19].

The scale of the PBG fiber is $L = 2.88753 \times 10^{-6}$ m. The wavelength we consider is $k = \frac{2\pi}{8.25} \times 10^7 \text{m}^{-1}$. The refractive index of the cladding and the outer region is $n_{\text{cladding}} = 1.45$, and the refractive index of the tubes is $n_{\text{tube}} = 1.8$. We have used a lattice with six dielectric rods, each with a (dimensionless) radius of $r_{\text{tube}} = 0.57142857$, encircling a fiber core of radius $r_{\text{core}} = 1.0$. The inner radius of the PML region is $r_{\text{outer}} = 3.80952380$, and the outer radius of the PML region is $r_{\text{PML}} = 5.80952380$.

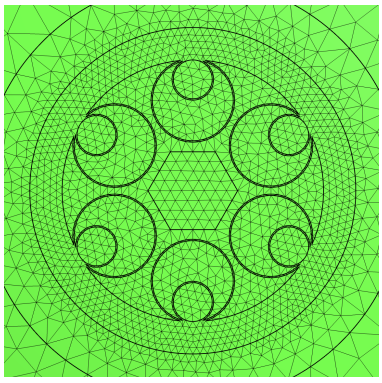

(a) Initial mesh for the NANF fiber.

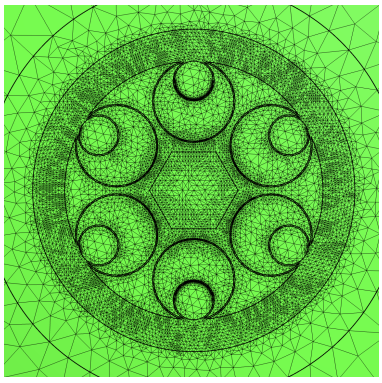

(b) Final mesh for the NANF fiber after the adaptive algorithm.

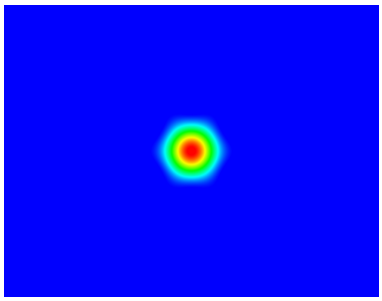

(c) Intensity of the full electric field (right eigenmode) at the final mesh.

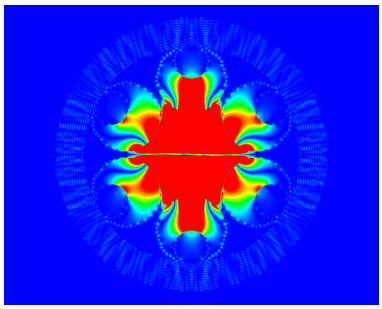

(d) Magnitude of the longitudinal component ($\varphi_h$) of the eigenmode.

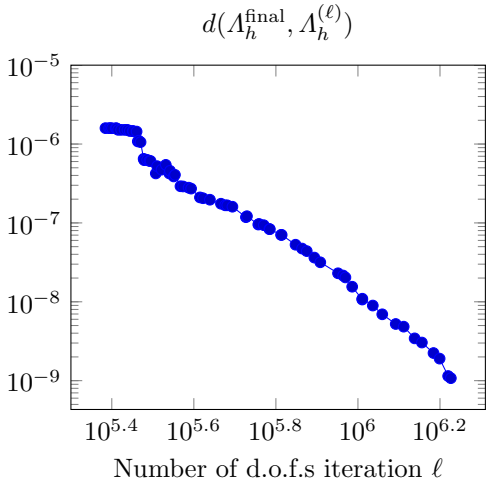


(e) History of adaptive convergence.

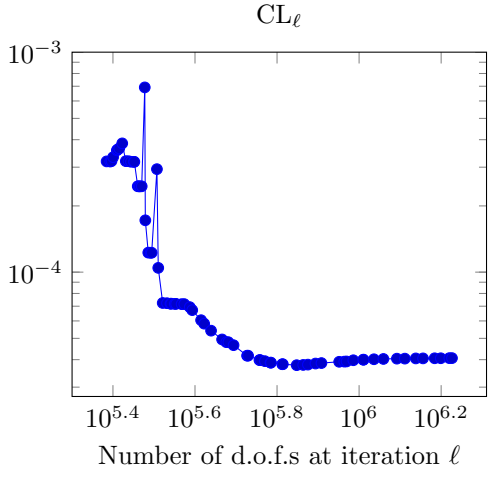


(f) History of computed loss values.

Figure 7: Results from the adaptive algorithm applied to NANF.

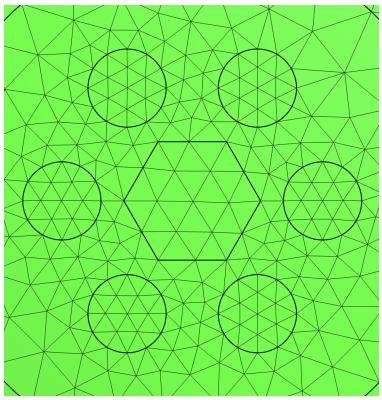

(a) Initial mesh for the PBG fiber, zoomed in near the core

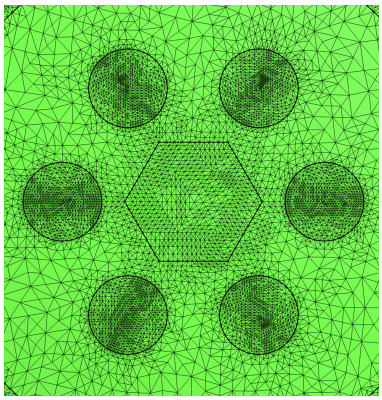

(b) Final mesh for the PBG fiber after the adaptive algorithm.

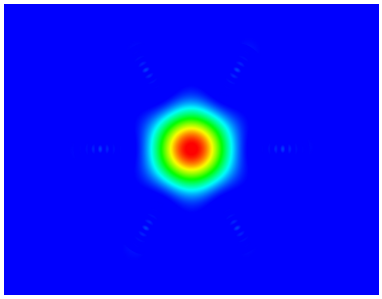

(c) Intensity of the full electric field (right eigenmode) at the final mesh.

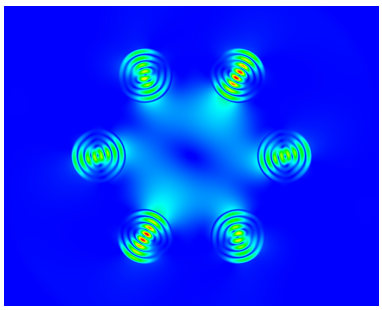

(d) Magnitude of the longitudinal component ($\varphi_h$) of the eigenmode.

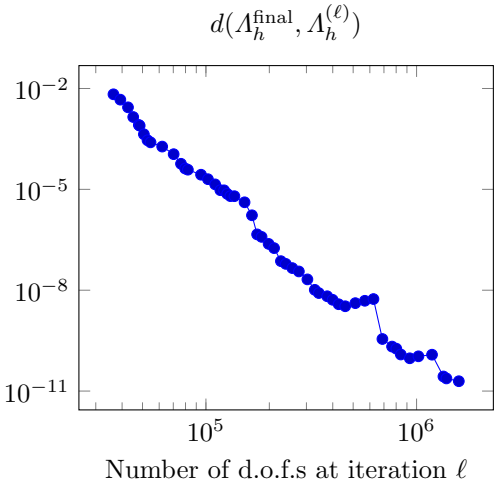


(e) History of adaptive convergence.

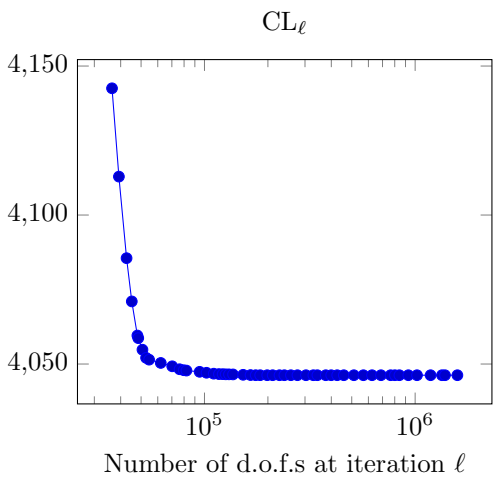


(f) History of computed loss values.

Figure 8: Results from the adaptive algorithm applied to the PBG fiber.

The results are in Figure 8. The initial mesh (Figure 8a) is relatively coarse, although we employed smaller elements in the core (with $h \approx 0.25$). For this fiber, as seen from Figure 8b, the adaptive process targets refinement within the dielectric rods that surround the solid dielectric core. We see finer scale ripples within these rods being resolved in Figure 8d. Again, these are better seen in the longitudinal component, and are hardly visible in the total intensity plot (in Figure 8c). The convergence of the eigenvalues during the adaptive process depicted in Figure 8e shows a monotonic descent, unlike what was found for the anti-resonant fibers (and like the prior cases, the discrete cluster $\Lambda_h^{(\ell)}$ here generally had two elements). The convergence of CL values is seen in Figure 8f.

To summarize the observations in this section, we have seen three examples of modern microstructured optical fibers, where our adaptive algorithm captured certain fine-scale modal features within the microstructures. We have also seen that without sufficient refinement in certain (perhaps unexpected) areas of the fiber geometry, the computed mode losses could be highly inaccurate.

**Disclaimers.** This article has been approved for public release; distribution unlimited. Public Affairs release approval #AFRL-2024-1561. The views expressed in this article are those of the authors and do not necessarily reflect the official policy or position of the Department of the Air Force, the Department of Defense, or the U.S. government.

## REFERENCES

[1] R. Becker and R. Rannacher, *An optimal control approach to a posteriori error estimation in finite element methods*, Acta numerica, 10 (2001), pp. 1–102.

[2] J.-P. Berenger, *A perfectly matched layer for the absorption of electromagnetic waves*, Journal of computational physics, 114 (1994), pp. 185–200.

[3] D. Bird, *Attenuation of model hollow-core, anti-resonant fibres*, Optics express, 25 (2017), pp. 23215–23237.

[4] T. D. Bradley, J. R. Hayes, Y. Chen, G. T. Jasion, S. R. Sandoghchi, R. Slavík, E. N. Fokoua, S. Bawn, H. Sakr, I. A. Davidson, et al., *Record low-loss 1.3 db/km data transmitting antiresonant hollow core fibre*, in 2018 European Conference on Optical Communication (ECOC), IEEE, 2018, pp. 1–3.

[5] F. Collino and P. Monk, *The perfectly matched layer in curvilinear coordinates*, SIAM J. Sci. Comput., 19 (1998), pp. 2061–2090 (electronic).

[6] C. M. B. Cordeiro, A. K. L. Ng, and H. Ebendorff-Heidepriem, *Ultra-simplified single-step fabrication of microstructured optical fiber*, Scientific Reports, 10 (2020), p. 9678.

[7] R. Cregan, B. Mangan, J. Knight, T. Birks, P. S. J. Russell, P. Roberts, and D. Allan, *Single-mode photonic band gap guidance of light in air*, science, 285 (1999), pp. 1537–1539.

[8] M. A. Duguay, Y. Kokubun, and T. L. Koch, *Antiresonant reflecting optical waveguides in $SiO_2$-Si multilayer structures*, Appl. Phys. Lett., 49 (1986).

[9] J. Gopalakrishnan, L. Grubišić, and J. Ovall, *Spectral discretization errors in filtered subspace iteration*, Mathematics of Computation, 89 (2020), pp. 203–228.

[10] J. Gopalakrishnan, B. Q. Parker, and P. Vandenberge, *Computing leaky modes of optical fibers using a FEAST algorithm for polynomial eigenproblems*, Wave Motion, 108 (2022), p. 102826.

[11] G. Gu, F. Kong, T. W. Hawkins, M. Jones, and L. Dong, *Extending mode areas of single-mode all-solid photonic bandgap fibers*, Opt. Express, 23 (2015), pp. 9147–9156.

[12] V. Heuveline and R. Rannacher, *A posteriori error control for finite element approximations of elliptic eigenvalue problems*, Advances in Computational Mathematics, 15 (2001), pp. 107–138.

[13] S. Kim and J. E. Pasciak, *The computation of resonances in open systems using a perfectly matched layer*, Mathematics of Computation, 78 (2009), pp. 1375–11398.

[14] J. C. Knight, *Photonic crystal fibres*, Nature, 424 (2003), pp. 847–851.
[15] A. N. Kolyadin, A. F. Kosolapov, A. D. Pryamikov, A. S. Biriukov, V. G. Plotnichenko, and E. M. Dianov, *Light transmission in negative curvature hollow core fiber in extremely high material loss region*, Optics express, 21 (2013), pp. 9514–9519.
[16] M. Koshiba and K. Inoue, *Simple and efficient finite-element analysis of microwave and optical waveguides*, IEEE Transactions on Microwave Theory and Techniques, 40 (1992), pp. 371–377.
[17] J. F. Lee, D. K. Sun, and Z. J. Cendes, *Tangential vector finite elements for electromagnetic field computation*, IEEE Transactions on Magnetics, 27 (1991), pp. 4032–4035.
[18] N. M. Litchinitser, A. K. Abeeluck, C. Headley, and B. J. Eggleton, *Antiresonant reflecting photonic crystal optical waveguides*, Optics Letters, 27 (2002), pp. 1592–1594.
[19] N. M. Litchinitser, S. C. Dunn, B. Usner, B. J. Eggleton, T. P. White, R. C. McPhedran, and C. M. de Sterke, *Resonances in microstructured optical waveguides*, Optics Express, 11 (2003), pp. 1243–1251.
[20] P. Monk, *Finite element methods for Maxwell's equations*, Oxford University Press, 2003.
[21] L. Nannen and M. Wess, *Computing scattering resonances using perfectly matched layers with frequency dependent scaling functions*, BIT Numer Math, 58 (2018), pp. 373–395.
[22] Y. Ohtera, H. Hirose, and H. Yamada, *Characteristics of resonantly-guided modes in microstructured optical fibers*, Photonics, 1 (2014), pp. 432–441.
[23] F. Poletti, *Nested antiresonant nodeless hollow core fiber*, Optics express, 22 (2014), pp. 23807–23828.
[24] F. Poletti, M. N. Petrovich, and D. J. Richardson, *Hollow-core photonic bandgap fibers: technology and applications*, Nanophotonics, 2 (2013), pp. 315–340.
[25] E. Polizzi, *Density-matrix-based algorithm for solving eigenvalue problems*, Physical Review B, 79 (2009), p. 115112.
[26] R. Rannacher, A. Westenberger, and W. Wollner, *Adaptive finite element solution of eigenvalue problems: Balancing of discretization and iteration error*, Journal of Numerical Mathematics, 18 (2010), pp. 303–327.
[27] J. Schöberl, *A posteriori error estimates for Maxwell equations*, Math. Comp., 77 (2008), pp. 633–649.
[28] J. Schöberl et al., *NGSolve: An open source finite element software library with C++ and Python interfaces*. http://ngsolve.org.
[29] L. R. Scott and S. Zhang, *Finite element interpolation of nonsmooth functions satisfying boundary conditions*, Math. Comp., 54 (1990), pp. 483–493.
[30] A. W. Snyder and J. D. Love, *Optical Waveguide Theory*, Kluwer Academic Publishers, 1983.
[31] P. Vandenberge, J. Gopalakrishnan, and J. Grosek, *Sensitivity of confinement losses in optical fibers to modeling approach*, Optics Express, 31 (2023), pp. 26735–26756.
[32] L. Vardapetyan and L. Demkowicz, *Full-wave analysis of dielectric waveguides at a given frequency*, Math. Comp., 72 (2003), pp. 105–129 (electronic).
[33] R. Verfürth, *A posteriori error estimation and adaptive mesh-refinement techniques*, Journal of Computational and Applied Mathematics, 50 (1994), pp. 67–83.
[34] P. Yeh and A. Yariv, *Bragg reflection waveguides*, Optics Communications, 19 (1976), pp. 427–430.
[35] L. Zschiedrich, S. Burger, J. Pomplun, and F. Schmidt, *Goal oriented adaptive finite element method for precise simulation of optical components*, in Integrated Optics: Devices, Materials, and Technologies XI, vol. 6475, SPIE, 2007, pp. 132–140.